# Western Arctic Primary Productivity Regulated By Shelf-break Warm Eddies

Eiji Watanabe[1]

Michio J. Kishi[1,2]

Akio Ishida[1,3]

Maki Noguchi Aita[1,2]

E. Watanabe: Japan Agency for Marine-Earth Science and Technology, 3173-25, Showa-machi, Kanazawa-ku, Yokohama, Kanagawa, 236-0001, JAPAN (Tel: +81-45-778-5675, email: ejn-abe@jamstec.go.jp)

[1]Japan Agency for Marine-Earth Science
and Technology, 3173-25, Showa-machi,
Kanazawa-ku, Yokohama, Kanagawa,
236-0001, JAPAN

[2]School of Fisheries Sciences, Hokkaido
University, N13 W8, Sapporo, Hokkaido,
060-0813, JAPAN

[3]Department of Social Environment, Fuji
Tokoha University, 325 Ohbuchi, Fuji,
Shizuoka, 417-0801, JAPAN

## Abstract

The response of phytoplankton to the Beaufort shelf-break eddies in the western Arctic Ocean is examined using the eddy-resolving coupled sea ice-ocean model including a lower-trophic marine ecosystem formulation. The regional model driven by the reanalysis 2003 atmospheric forcing from March to November captures the major spatial and temporal features of phytoplankton bloom following summertime sea ice retreat in the shallow Chukchi shelf and Barrow Canyon. The shelf-break warm eddies spawned north of the Barrow Canyon initially transport the Chukchi shelf water with high primary productivity toward the Canada Basin interior. In the eddy-developing period, the anti-cyclonic rotational flow along the outer edge of each eddy moving offshore occasionally traps the shelf water. The primary production inside the warm eddies is maintained by internal dynamics in the eddy-maturity period. In particular, the surface central area of an anti-cyclonic eddy acquires adequate light, nutrient, and warm environment for photosynthetic activity partly attributing to turbulent mixing with underlying nutrient-rich water. The simulated biogeochemical properties with the dominance of small-size phytoplankton inside the warm eddies are consistent with the observational findings in the western Arctic Ocean. It is also suggested that the light limitation before autumn sea ice freezing shuts down the primary production in the shelf-break eddies in spite of nutrient recovery. These results indicate that the time lag between the phytoplankton bloom in the shelf region following the summertime sea ice retreat and the eddy generation along

the Beaufort shelf break is an important index to determine biological regimes in the Canada Basin.

Keyword :

phytoplankton bloom

eddy dynamics

shelf-basin exchange

Pacific-origin water

a lower-trophic marine ecosystem model

## 1. Introduction

The influence of abrupt sea ice retreat on the Arctic marine ecosystem is a crucial topic in academic, commercial, and social communities [*Arrigo et al.*, 2008; *Pabi et al.*, 2008]. Recent satellite analysis indicated that high primary production region shifts northward from the Bering Sea to the Chukchi Sea following sea ice reduction [*Grebmeier et al.*, 2010]. While the systematic field campaign conducted in the Western Arctic Shelf-Basin Interaction (SBI) project has produced major important findings in the 2000s [*Grebmeier and Harvey*, 2005; *Grebmeier et al.*, 2009], an impact of ocean dynamics on polar biological cycles still has a lot of uncertainties. The Pacific-origin water inflowing from the Bering Strait is a predominant source of not only heat and fresh water, but also nitrate, silicate, dissolved- and particulate organic materials in the Arctic Ocean. The nutrient-rich Pacific water undergoes physical and biogeochemical modifications through seasonal primary production and interactions with organic-rich bottom sediments in the Chukchi shelf [*Weingartner et al.*, 2005]. The buoyant Pacific summer water flows along the Alaskan northwestern coast as a surface-intensified current, and its significant part is eventually transported into the Canada Basin by shelf-break eddies during late summer and early autumn [*Pickart*, 2004; *Watanabe and Hasumi*, 2009].

In the northern Gulf of Alaska, anti-cyclonic eddies propagating along a continental slope were frequently detected by satellite remote sensing [*Okkonen et al.*, 2003]. The eddy-like features of high chlorophyll-*a* (CHL) concentration implied that mesoscale eddies were carrying phytoplankton and nutrient from the outer shelf toward the deep basin. In *Ueno et al.* [2010], the role of the Alaskan Stream eddies in the CHL distribution in the

central subarctic North Pacific was categorized into three types: 1) the lateral transport of shelf-origin nutrient and biological organism via advection of eddy body and/or rotational circulation around of each eddy, 2) nutricline shallowing accompanied by eddy decay, and 3) Ekman upwelling induced by eddy-wind interaction. The latter two processes work on upward nutrient flux. Thus biological activities could be closely related to mesoscale eddies. In the western Arctic, eddy contribution to phytoplankton activities has not been fully evaluated yet. It is reported that the surface and halocline layers above 300 m depth in the Canada Basin are full of a number of anti-cyclonic eddies [*Manley and Hunkins*, 1985]. A major part of anti-cyclonic cold-core eddies are considered to be generated from a bottom-intensified current along the northern edge of Chukchi shelf via baroclinic instability in early spring [*Spall et al.*, 2008]. *Mathis et al.* [2007] and *Kadko et al.* [2008] suggested that a cold eddy observed on the Chukchi Sea continental slope played a crucial role in the transport of carbon, oxygen, and nutrient associated with the Pacific winter water. However, the cold-eddy intrusion into the halocline layer of Canada Basin hardly enforces primary production in the surface euphotic zone at once.

The surface-intensified warm-core eddies with the signal of the Pacific summer water are occasionally detected in the vicinity of the Barrow Canyon from later summer to early autumn [*Pickart*, 2004]. The detailed properties of a visible warm eddy observed by the R/V Mirai in 2010 were reported in *Nishino et al.* [2011a]. The buoyant warm-core eddy would efficiently supply the surface layer of basin interior with a great amount of ammonium produced by the decomposition of organic matters on the bottom of Chukchi Sea shelf during summer, although the annual nutrient transport of warm eddies might be much smaller than the contribution of cold eddies [*Nishino et al.*, 2005]. The eddy

transport of ammonium-rich shelf water could sustain locally enhanced growth of smaller-size phytoplankton in the southern Canada Basin. However, it is still unclear whether the eddy-like structures of biological signal attributed to the lateral advection of high phytoplankton biomass from the Chukchi and Beaufort shelf region or were formed by local biological primary production inside the eddies.

In recent years, numerical studies on the Arctic marine biology become activated. The impact of Arctic sea ice decline on the marine plankton ecosystem was also addressed using both global simulation products [*Popova et al.*, 2010; *Jin et al.*, 2011] and a pan-Arctic regional modeling [*Zhang et al.*, 2010]. According to their analyses, the primary productivity of phytoplankton over seasonal ice areas of the Arctic Ocean is enhanced primarily by the increases in photosynthetically active radiation and nutrient availability in the euphotic zone, and partially due to surface water warming. The strong mixing and upwelling associated with summertime sea ice reduction are dynamic drivers for nutrient retrieval. The spatial pattern of ice algae and the size distribution of pelagic phytoplankton groups were also reported [*Jin et al.*, 2011]. These models successfully reproduced the Arctic basin-scale features of CHL and primary production. On the other hand, several kinds of complexity on the shelf process and shelf-basin exchange for the analysis have commonly emerged owing to insufficient model resolution to explicitly resolve topographic ocean current, waves, and mesoscale eddies.

*Watanabe and Hasumi* [2009] and *Watanabe* [2011] examined 1) mechanisms controlling the hydrographic properties of the Beaufort shelf-break warm eddies and 2) the relationship of Pacific water transport with summertime sea ice extent and shelf-wide wind fields using an eddy-resolving coupled sea ice-ocean model covering the western Arctic Ocean.

These previous studies clarified that early sea ice retreat toward the Canada Basin and westerly surface wind over the Chukchi shelf promoted the shelf-to-basin transport of the Pacific summer water via enhanced eddy activities.

In this paper, the phytoplankton behaviors regulated by the shelf-break warm eddies are addressed using the high-resolution model newly coupled with a lower-trophic marine ecosystem formulation. We performed the model integration from March to November in the same framework as *Watanabe* [2011] and investigated the contribution of local dynamics, such as shelf-water transportation, turbulent mixing, and upwelling, to primary productivity following eddy life cycle in the Beaufort shelf-break region. The method of modeling analyses is described in section 2. The seasonal transitions in physical oceanographic fields and biological performance in the western Arctic Ocean are traced in section 3, and the eddy-related phytoplankton activities are then focused on in section 4. The findings obtained in the present work are summarized in section 5.

## 2. Model and Experimental Design

The coupled sea ice-ocean model used in the present work is composed of a physical ocean general circulation model named Center for Climate System Research Ocean Component Model (COCO) version 3.4 [*Hasumi*, 2006] and a lower-trophic marine ecosystem part named North Pacific Ecosystem Model for Understanding Regional Oceanography (NEMURO) [*Kishi et al.*, 2007]. The model domain contains the entire Chukchi Sea and the southern area of the Canada Basin (Figure 1a). The horizontal resolution is about 2.5 km, and there are 25 vertical levels. The physical oceanographic part of model and experimental design is the same as the 2003 case in *Watanabe* [2011] except the Bering Strait condition. In the previous experiments (i.e., *Watanabe and Hasumi* [2009]; *Watanabe* [2011]), the temperature of Bering Strait throughflow was prescribed to an idealized seasonal cycle, and the coldest water at the freezing point inflowed into the southern Chukchi shelf even after sea ice retreat in early summer. To prevent this inconsistent situation, the freezing period of inflow is shortened until May. The atmospheric forcing components are obtained from the National Centers for Environmental Prediction / National Center for Atmospheric Research reanalysis daily dataset in 2003 [*Kalnay et al.*, 1996].

The detailed configuration of NEMURO is described in *Kishi et al.* [2007]. The model treats the concentration of 11 biogeochemical variables illustrated in Figure 1b. While the NEMURO has been originally developed for the assessment of marine biology in the North Pacific, its reasonable performance was recently confirmed even in the global domain [*Sumata et al.*, 2010; *Kishi et al.*, 2011] and in the Arctic basin-scale primary productivity [*Zhang et al.*, 2010]. In our experiments, the parameter values such as the photosynthetic rate of phytoplankton and the grazing rate of zooplankton basically follow

*Zhang et al.* [2010]. Their modification of model structure from *Kishi et al.* [2007] (i.e., ZS grazing on PL in Figure 1b) is not incorporated, because we do not still have established findings on zooplankton behaviors in the Arctic Ocean. Instead, a sensitivity experiment on zooplankton impact is conducted as an extreme case (see section 5). The sea ice ecosystem with ice algae, nutrient exchange via ice-ocean interface, and light penetration through ice column are neglected for simplicity.

As demonstrated in *Watanabe and Hasumi* [2009], the Pacific water transport across the Chukchi and Beaufort shelf breaks reaches a maximum from late summer to early autumn and becomes a minimum in mid-winter. In addition, we focus on summertime biological activities, especially the impact of shelf-break warm eddies on phytoplankton dynamics. The model is hence integrated for 9 months from March to November. The experiment has no spin-up stage to minimize the disturbance of hydrographic structure in the Canada Basin due to the closed lateral boundary of model domain. This integration period is regarded to cover the annual bloom event. The model is initiated from temperature and salinity fields in the Polar Science Center Hydrographic Climatology (PHC) March data [*Steele et al.*, 2001], arbitrary sea ice thickness constructed by multiplying a factor of 1 m to the climatological mean sea ice concentration [*National Ice Center*, 2006], no circulation of both sea ice and ocean following *Watanabe* [2011]. The monthly climatology data of nitrate and silicate concentration derived from the World Ocean Atlas 2009 (WOA09) [*Garcia et al.*, 2010] are utilized for restoring along the lateral boundary region of model domain, and its March values are given to the initial fields. Nutrient supply from river water discharge is not taken into account, because its influence on primary productivity would be localized in the vicinity of each river mouth [*Wang et al.*, 2005].

To indirectly account for ammonium dissolution from sea bottom sediments, ammonium concentration in the deepest layer on the entire shelf where the water depth is shallower than 200 m is restored to seasonally varying amount with the annual average of 2 $\mu$M ($1\,\mu\mathrm{M} \equiv 1\,\mathrm{mmolN\,m^{-3}}$). The idealized seasonal cycle with the maximum value of 4 $\mu$M in August and the minimum value of 0 $\mu$M in February is prescribed based on previous observations [*Nishino et al.*, 2005]. Initial phytoplankton and zooplankton biomass is uniformly distributed in the upper 200 m of the entire domain. The initial concentration of 0.02 $\mu$M is approximately two-order smaller than the simulated phytoplankton biomass during the blooming period (see section 3). The initial value of other components is set to quite low value. The experiment described above is named the 2003 case, hereafter.

The simulated sea ice concentration is compared with the Advanced Microwave Scanning Radiometer for Earth Observing System (AMSR-E) data set, which is available at the International Arctic Research Center of the University of Alaska Fairbanks (IARC) - Japan Aerospace Exploration Agency (JAXA) Information System (IJIS) data archive. The 2003 July average is shown in section 3.1. For the comparison of phytoplankton distribution, the spatial features of summertime CHL concentration in the western Arctic Ocean are checked using the monthly and 8-day composites of Moderate-Resolution Imaging Spectroradiometer (MODIS). The scenes with a spatial resolution of 4 km are downloaded from the National Aeronautics and Space Administration (NASA) ocean color website [http://oceancolor.gsfc.nasa.gov] and are digitally processed using the NASA's Sea-Viewing Wide Field-of-View Sensor (SeaWiFS) Data Analysis System (SeaDAS) software as in *Watanabe* [2011]. Since the detection of local particular signals from satellite ocean-color sensor is difficult owing to numerous missing values under cloud-cover condi-

tion in the western Arctic region, we pick up the 2003 July composite for the shelf field in section 3.1 and two examples of 2003 and 2010 weekly composites for the eddy field in section 4.1. In this paper, we assume 1 mmolN $\sim$ 80 mgC $\sim$ 1.6 mgChl based on the mass ratio C/CHL of 50 and the Redfield ratio C/N of 6.625 for comparison between the model output and the observational estimate with different units, as in *Aita et al.* [2007].

## 3. Phytoplankton Activity in the Western Arctic Ocean

### 3.1. Model Performance on Phytoplankton Bloom Before Eddy Generation

The overall spatial pattern in the 2003 case is documented including comparison with previous observational findings. As described in *Watanabe* [2011], the sea ice extent, sea surface temperature (SST), sea surface height, shelf-wide and basin-scale sea ice and ocean circulation fields are mostly reproduced. From March to May, the wide area of model domain is covered by sea ice. In June, an initial phytoplankton bloom occurs following the summertime sea ice retreat in the Chukchi shelf. The surface phytoplankton concentration on July 1 captures the high biomass band along sea ice margin over the northern edge of Chukchi Sea and north of the Alaskan northern coast, where the sea ice extent is consistent with the AMSR-E scene (Figures 2a-b).

The quite low concentration appears in the northeastern Chukchi shelf from the Cape Lisburne to the Barrow Canyon. Figure 3 displays the vertical profile of phytoplankton and nitrate concentration along the meridional section from the Bering Strait to the Northwind Ridge on the same day as Figure 2a. The profile is characterized by the subsurface maximum of phytoplankton biomass reaching 4 $\mu$M over the northern Chukchi shelf (70°N - 73°N). The subsurface maximum is accompanied by the deepening of nutricline and can be simply explained by a combination of nutrient limitation and light availability, since the half saturation constant for nitrate is set to 0.7 $\mu$M for both small (PS) and large (PL) phytoplankton following *Zhang et al.* [2010]. Actually, most of nitrate in the surface euphotic zone of central Chukchi shelf is depleted owing to the initial bloom after sea ice opening by the end of June. The depression of iso-nitrate contours in this region is captured by the WOA09 July climatology (Figure 3). In the same period, a significant part of

phytoplankton biomass diminished via northward advection [*Hill et al.*, 2005; *Watanabe*, 2011] and local biological process (i.e., mortality, grazing of zooplankton etc.). On the other hand, the warm and nutrient-rich Pacific water inflowing from the Bering Strait continuously sustains the phytoplankton bloom in the southern Chukchi shelf, where the southward increase in surface CHL concentration was detected by the MODIS July composite in 2003 (Figures 2a-b). The vertically integrated PS and PL biomass reaches 366 $\mu$M m ($\sim$ 586 mgChl m$^{-2}$) at the Bering Strait in the 2003 case. In reality, the high nitrate concentration over 10 $\mu$M and the CHL content up to 734 mgChl m$^{-2}$ were observed at the strait during the 2002 - 2004 cruises [*Lee et al.*, 2007].

Another feature in Figure 2a is lower phytoplankton biomass in the central Canada Basin than that over the Chukchi Plateau, although both the regions are still covered by sea ice packs. The remarkable deepening of nutricline via Ekman downwelling associated with the Beaufort High sea level pressure would account for the restricted primary production in the central basin [*Nishino et al.*, 2011b; *Watanabe*, 2012]. The nitrate concentration over the Northwind Ridge is somewhat lower than the WOA09 July climatological composite (Figure 3), presumably because the wider sea ice opening than the multi-decadal average promoted the nitrate uptake associated with primary production for the recent years. In addition, we should consider that the original data of WOA09 with the coarse resolution of $1^\circ \times 1^\circ$ have difficulty in capturing local features. It is also found that the initial bloom is dominated by PL in the entire domain, and the PS habitat is limited to the Alaskan coastal region south of the Cape Lisburne at the beginning of July (see yellow contours in Figure 2a).

### 3.2. Seasonal Transition in the Barrow Canyon

The Barrow Canyon is an important passage for the transport of Pacific summer water from the Chukchi shelf to the Canada Basin. Since the Pacific summer water is a major source of the Beaufort shelf-break warm eddies, the water mass properties in the canyon would significantly control biological regimes in the basin. The physical and biogeochemical properties in the canyon are investigated hereafter in this subsection. The Barrow Canyon is dominated by strong northeastward ocean current, and the major variations in plankton biomass and nutrient amount in the canyon represent the biological activity in the upstream regions over the Chukchi shelf. It should be hence noted that the changes in the Barrow Canyon are not immediately recovered even when water mass is continuously replaced via advection.

The temporal variability of vertically cumulative phyto- and zooplankton biomass, SST, surface light availability, sea ice concentration, and nutrient concentration are plotted in Figure 4. The readers can check the exact formulation and parameter values of primary production rate adopted in the 2003 case in Appendix. All the daily values are their averages in the Barrow Canyon section (Figure 2a), which is defined by a line between a location northwest of the canyon (156.6°W, 71.9°N) and Point Barrow (156.3°W, 71.3°N) as same as *Watanabe* [2011]. First, it is found that there are remarkable differences in the seasonal variations between PS and PL (Figure 4a). PL biomass initially breaks up at the end of April and reaches its peak of 82 $\mu$M m ($\sim$ 6.6 gC m$^{-2}$) in the early period of June. After then, PL biomass gradually decreases without its distinct peak until the finish of model integration. PS biomass slowly increases from May, but overtakes PL biomass at the end of July. The seasonal variation in ZL biomass follows these phytoplankton

behaviors via grazing process (Figure 4b). ZL biomass averaged in the Barrow Canyon increases from June to July, and has a peak of 50 $\mu$M m ($\sim$ 4.0 gC m$^{-2}$) at the beginning of August, when a significant amounts of PS and PL are both alive. To the contrary, ZS biomass is quite low throughout the blooming season. ZP biomass slightly increases after July, but the amount is evidently low relative to ZL. *Campbell et al.* [2009] estimated that the total copepod biomass in the upper 100 m of northern Chukchi shelf region seasonally changed from 0.6 gC m$^{-2}$ in May - June to 1.9 gC m$^{-2}$ in July - August, 2002. Since the ZL biomass recalculated in the top 100 m is 45 $\mu$M m ($\sim$ 3.6 gC m$^{-2}$) in the 2003 case, the model result may overestimate the ZL grazing on phytoplankton species. The impact of zooplankton is discussed in section 5.

SST is kept at the freezing point until May and then suddenly rises up to 6°C within two weeks in June (Figure 4c). The rapid warming corresponds to sea ice removal from the canyon. The surface light availability (SLA) is also principally synchronized with sea ice concentration over the canyon (Figure 4d). The non-zero value of SLA even with freezing SST during the spring season means the partial exposure of open water area. The SLA drop in early July reflects the photoinhibition of phytoplankton for the annual maximum period of solar radiation. While the simulated light property depends on the parameter values of P-E curve (see Appendix), the summertime photoinhibition of diatom group was at least reported in the southeastern Beaufort Sea [*Palmer et al.*, 2011]. In August and September, when the SLA fluctuates just below the maximum value of 1, photosynthesis is not completely restricted by light intensity in the surface layer.

The vertical profile along the Barrow Canyon section on June 11, when the PL biomass maximum is recorded, is shown in Figure 5. The LA term vertically lapses to 0.1 at 30 - 50

m depth and 0.01 at 60 - 100 m depth. The light extinction rate depends on self-shading effect of phytoplankton biomass in addition to a water depth [*Kishi et al.*, 2007]. The high PL biomass dominates the upper 30 m, where nitrate uptake has been considerably progressed since sea ice opening. Recalling the half saturation constant of 0.7 $\mu$M, the profile indicates that nitrate is still available for photosynthesis even below the depth of PL biomass maximum. Another feature is the east-west gradient of PL and nitrate concentration below the 40 m depth. PL biomass substantially resides in the eastern side of the canyon (i.e., the Alaskan coastal side). This distribution is accompanied by nutrient consumed in the upstream region and reflects the pathway of Pacific summer water, as shown in the ship-based measurements [*Walsh et al.*, 2011] and in the tracer experiment [*Watanabe and Hasumi*, 2009].

Here, we consider the nutrient concentration multiplied by the light availability in each horizontal and vertical grid in order to filter out the value in the dark layer (Figure 4e). For example, light-weighted nutrient concentration is nearly zero due to full ice cover regardless of nutrient amount in March. The multiplied value in each grid is also averaged through the entire water column. The optimized nitrate concentration abruptly drops in early May after its maximum of 0.29 $\mu$M due to phytoplankton bloom, while a part of the depression is explained by the weakened light condition during May 5 - 8. In the case of June 11, the value records 0.06 $\mu$M (cf. Figure 5). The ammonium concentration is low until the end of May, but the gradual increase is then induced by the modeled remineralization processes and the restoring in the deepest layer. The effect of bottom flux is referred in section 5. The silicate variation traces similar features with nitrate concentration before August and then becomes gradually reduced in contrast to nitrate

regeneration via nitrification in late summer (Figures 4e-f). The surface nitrate depletion, the subsurface maximum of phytoplankton biomass above 2 $\mu$M ($\sim 3.2\,\mathrm{mgChl\,m^{-3}}$) located at the 20 - 40 m depth, and the dominance of larger-size diatom in the entire canyon column after the early bloom are consistent with the SBI measurements [*Hill et al.*, 2005; *Sukhanova et al.*, 2009], although the greatest value of CHL concentration up to 12 $\mathrm{mgChl\,m^{-3}}$ observed in their cruises is not reproduced in our experiment.

Based on each time series described above, the phytoplankton growth in the Chukchi shelf before the eddy generation period are summarized (see also Appendix). Solar input with sea ice retreat initializes the phytoplankton bloom. The SST increase of 8°C provides the Tmp term with 1.74 times larger contribution to photosynthesis following the so called $Q_{10}$ relationship. The delayed growth of PS relative to PL is explained by the difference in parameter values of maximum photosynthetic rate ($V_{max}$) as long as enough nutrient is available for uptake. The silicate depletion in the surface layer gradually inhibits the PL growth in early summer, while PS can continue to grow up with the uptake of nitrate and ammonium even in late summer. Actually, the similar seasonal shift of dominant species to smaller-size phytoplankton groups was observed by *Hill et al.* [2005]. Thus when the Beaufort shelf-break eddies are initially generated in late July, the changes in PL and PS biomass in the Barrow Canyon are negative and positive, contrastively. The gross primary production rate of PL (GppPL) and PS (GppPS) with the peak of nearly 8 $\mu\mathrm{M\,m\,day^{-1}}$ ($\sim 0.64\ \mathrm{gC\,m^{-2}\,day^{-1}}$) shown in Figure 4g fundamentally changes in phase with the biomass of PL and PS itself and is modified by nutrient environment including the high efficiency of ammonium uptake (cf., characterized by lower half saturation constant for ammonium). It is expected that these seasonal variations would be closely

linked to the primary productivity in the Beaufort shelf-break warm eddies unless nutrient compensation occurs in the downstream region.

## 4. Phytoplankton Behaviors associated with Beaufort Shelf-break Eddies

### 4.1. Eddy-like Structure of Phytoplankton Biomass

In August, a few anti-cyclones spawned from the Barrow Canyon jet and eastward shelf-break current intrude into the basin interior [*Watanabe*, 2011]. The spatial distribution of combined PS and PL biomass illustrate the swirling structure north of the Barrow Canyon (Figure 6a). The phytoplankton biomass is clearly higher in an individual eddy than the surrounding basin area. We found that two examples of MODIS CHL distribution among all weekly composites from 2003 to 2008 were most visible as introduced in section 2. First, the eddy-like feature of high CHL concentration appeared north of the Beaufort shelf break on September 6 - 13, 2003 (Figure 6b), when the warm eddies were detected by the MODIS 11-$\mu$m brightness temperature [*Watanabe*, 2011]. The maximum value of CHL concentration reaches 0.3 $\mu$M ($\sim$ 0.5 mgChl m$^{-3}$) at 145°W and 71°N. The other feature of eddy-like CHL distribution was captured northwest of Point Barrow on August 21 - 28, 2010 (Figure 6c). The maximum CHL concentration records 0.9 $\mu$M ($\sim$ 1.5 mgChl m$^{-3}$) at 158°W and 74°N. This location is close to the distinct warm eddy tracked by the R/V Mirai cruise during late summer and early autumn in the same year [*Nishino et al.*, 2011a]. The maximum value of surface phytoplankton concentration on August 27 in the 2003 case corresponds to 0.4 $\mu$M (0.6 mgChl m$^{-3}$) (Figure 6a), which is in the same order as the MODIS values and the observed CHL concentration up to 0.8 mgChl m$^{-3}$ in *Nishino et al.* [2011a] (Figure 3c in their paper).

### 4.2. Eddy Generation/Development Stage

The daily primary production rate in the Beaufort shelf-break region is tracked following the eddy life stages (Figure 7). When the shelf-break warm eddies are initially generated at the end of July, the eddy-like distribution of shelf-origin water with high primary productivity arises north of the Barrow Canyon (Figure 7a). These anti-cyclonic eddies migrate offshore with developing their sizes in August (Figure 7b). Even though several weeks have passed from its generation, apparent primary production still continues at the eddy center. In addition, the western July eddy (named JED) traps the shelf water along the outer edge of eddy via clockwise rotational flow.

To estimate the relative importance of shelf-water transport on primary productivity inside the shelf-break eddies, we conducted an idealized experiment. In the original 2003 case, a virtual passive tracer associated with the Pacific-origin water is provided at the Bering Strait so that the tracer concentration is kept at 100% at the strait throughout the integration period. The readers can confirm the overall distribution of Pacific water tracer in *Watanabe* [2011] and the offshore intrusion accompanied with the JED in Figure 7a. In the "No Basin Biogeochemical Value (NBBV)" case, all values of 11 biogeochemical components of NEMURO (Figure 1b) are reset to zero on July 24 in the basin-side area where the concentration of Pacific water tracer is below 0.1 in each vertical level on the same day (see blue contours in Figure 7a). The modified integration from July 24 to August 27 results in the similar spatial pattern of gross primary production rate including the eddy-like maximum, although the magnitude is slightly smaller compared with the 2003 case (Figures 7b and 8). Therefore, it can be regarded that the primary productivity inside the JED is maintained by consuming the residual of nutrient taken at the initial

eddy stage and that the exchange of biogeochemical properties with background basin environment is not an essential process.

### 4.3. Eddy Maturity Stage

The primary production inside the JED is enhanced when the eddy activities become prominent in September (Figure 7c). It can be also detected that a newly generated eddy north of the Barrow Canyon (named SED) transports the Chukchi shelf water with high primary productivity. The vertical profiles of primary production rate, nitrate concentration, and vertical diffusivity/velocity across the JED and SED are shown in Figure 9. The eddy properties are characterized by the lower nitrate concentration, which is below 1 $\mu$M at the depth shallower than 80 m at the eddy center as observed in late summer 2010 *Nishino et al.* [2011a]. It is sometimes reported that the depression of nutricline restricts primary production in an anti-cyclonic eddy [*Ueno et al.*, 2010]. On the other hand, the model result shows a hot spot of production in the inner uppermost layer.

GppPS at the center of JED in the surface layer is $6.86 \times 10^{-2}\,\mu\mathrm{M\,day^{-1}}$ on September 19, which is two order of magnitude greater than that of $0.01 \times 10^{-2}\,\mu\mathrm{M\,day^{-1}}$ at the surface eddy edge (Figure 9c and Table 1). The relative contribution of nutrient uptake, temperature-dependent, and light availability terms to GppPS is compared between the center and edge of JED at the ocean surface. Evidently, the eddy center has higher nitrate, ammonium, and water temperature than the eddy edge. The Michaelis-Menten formulation with the gourmet term of ammonium intends that the higher anomalies of nitrate (0.13 $\mu$M) and ammonium (0.07 $\mu$M) result in an order greater contribution to GppPS. The $Q_{10}$ relationship prescribes that the warm anomaly of 2°C is equivalent to 20% larger increases in GppPS as well. The horizontal gradient of surface light availability is negligible for photosynthesis on the eddy scale of $O(10$ km). While the upper column of eddy center has quasi-uniform nutrient and temperature condition, GppPS of $0.93 \times$

$10^{-2}\,\mu\mathrm{M\,day}^{-1}$ in the subsurface layer is significantly smaller than at the ocean surface (Figure 9c and Table 1). The vertical contrast of GppPS is simply explained by surface light availability that is eight times higher than that at the 60 m depth. Therefore, the surface central area of shelf-break warm eddies satisfies enough light, nitrate/ammonium, and high-temperature environments, which are all suitable for PS photosynthetic activity. A key point here is that the primary production of PL is constrained even at the surface eddy center in contrast to the seasonal dominance in the basin subsurface layer (Figure 9d). Since the light, nitrogenous nutrient (nitrate and ammonium), and temperature conditions including parameter values for PS and PL are same, the lower GppPL is explained by the limited silicate uptake. In fact, the residual silicate concentration is quite low on the pathway of shelf-origin water through the Barrow Canyon (Figure 4f) and inside the eddies (Table 1). The demonstrated water temperature and predominance of smaller-size phytoplankton species are consistent with the in-situ measurements conducted by the R/V Mirai 2010 cruise [*Nishino et al.*, 2011a].

The roles of internal eddy dynamics, such as vertical mixing and local upwelling/downwelling, in nutrient redistribution and the consequent regulation of primary productivity are analyzed. Figure 9e indicates that the enlarged vertical diffusivity up to $2.7 \times 10^{-2}\,\mathrm{m^2\,s^{-1}}$ in the upper 80 m of JED center drives the exchange with underlying nutrient-rich water that is also shelf-origin. The localized high vertical diffusivity is comparable with the tidal mixing of $O(10^{-2}\,\mathrm{m^2\,s^{-1}})$ reported around the Kuril Strait in the North Pacific [*Kawasaki and Hasumi*, 2010]. In the COCO model, the vertical diffusion coefficient is diagnosed using the turbulence closure scheme of *Noh and Kim* [1999] at each time step. The turbulent kinetic energy inside the shelf-break eddies arises

410 according to the vertical shear of horizontal velocity and is maintained for the sake of
411 weakened stratification. Another features of eddy dynamics include the upward nutrient
412 shift induced by upwelling flow that reaches 6.2 m day$^{-1}$ in the outer side of JED (Figure
413 9e). The upwelling/downwelling event is recognized as the perturbation of eddy activi-
414 ties, since the daily fluctuation of vertical velocity is not synchronized with the Ekman
415 convergence/divergence derived from surface wind stress (Figure 9b).

416 To evaluate the impact of these eddy processes on GppPS and GppPL, we conducted
417 sensitivity experiments where nitrate, ammonium, and silicate redistribution caused by
418 each of vertical diffusion and advection flux terms is excluded during the model integration
419 from August 27 to September 19. These idealized experiments are named "No Vertical
420 Nutrient Diffusion (NVND)" and "No Vertical Nutrient Advection (NVNA)" cases, re-
421 spectively. In the NVNA case, the vertical component of nutrient advection parts written
422 in the flux form is set to zero at all layer boundaries for the conservation of total nutrient
423 content in this calculation. The other model part including physical fields is identical
424 to the 2003 case. The simulated eddy fields in the NVND case are characterized by the
425 nutricline shoaling and the reduction of primary productivity in the central column of
426 JED (Figures 10a-b). The decrease in net upward nutrient flux accounts for the GppPS
427 (GppPL) decrease to $1.64 \times 10^{-2}$ ($0.21 \times 10^{-2}$) $\mu$M day$^{-1}$ at the surface eddy center. At
428 the same time, the increase rate of GppPS (GppPL) to $1.43 \times 10^{-2}$ ($0.18 \times 10^{-2}$) $\mu$M day$^{-1}$
429 accompanied by the positive anomaly of nutrient concentration is small due to limited
430 light availability at the subsurface eddy center (Table 1). Thus it is confirmed that the
431 primary production inside the shelf-break warm eddies is enhanced by turbulent mixing
432 even a few months after their generation, and the magnitude is comparable with the sea-

sonal subsurface maximum in the basin interior (Figures 9c-d). In contrast, the deviation of GppPS and GppPL in the NVNA case from the 2003 case is small inside the JED relative to that in the NVND case (Figures 10c-d, Table 1). The result suggests that the nutrient redistribution due to local upwelling/downwelling event has a minor contribution to the primary productivity of shelf-break eddies. The large negative anomaly of GppPL at the nutricline depth of basin interior is expected to be explained in part by the lack of wind-driven upwelling of underlying nitrate-rich water, while such basin processes are out of the scope in this study.

### 4.4. Eddy Decay Stage

There is a few reports on the shoaling of nutricline inside the anti-cyclonic eddies according to their decay and the corresponding restart of active primary production in the North Pacific [*Ueno et al.*, 2010]. On the other hand, the model result in the 2003 case shows weakened primary productivity in the southern Beaufort Sea in October (Figure 7d), when the vorticity of shelf-break warm eddies gradually shrinks due to lateral friction [*Watanabe*, 2011]. The AMSR-E sea ice monitor indicated that the ice freezing period in the southern Beaufort Sea started during October and November every year in the 2000s [http://www.ijis.iarc.uaf.edu/cgi-bin/seaice-monitor.cgi]. The autumn sea ice spread normally precedes the disappearance of shelf-break warm eddies, and the further eddy shrinking then occurs due to sea ice drag in addition to lateral friction. In the 2003 case, sea ice freezing prevents light absorption at the ocean surface and ceases the primary production of pelagic phytoplankton species in the most shelf-break region in mid-October. An exceptional area appears in the vicinity of JED centered at 153°W and 73°N (see the location in Figure 7d). The local delay of sea ice freezing until November 8 occurs attributing to ocean heat content inside the JED. To confirm whether open water exposure over the shelf-break warm eddies can prolong the photosynthesis period or not in the southern Beaufort Sea, the JED properties are compared between the eddy maturity and decay periods (Figure 11).

The temporal changes are characterized by the remarkable decline of GppPS from $6.86 \times 10^{-2}\,\mu\mathrm{M\,day^{-1}}$ on September 19 to $0.18 \times 10^{-2}\,\mu\mathrm{M\,day^{-1}}$ on October 31 at the surface eddy center. The following values are also taken at the same place. During this period, nitrate (ammonium) concentration recovers from 0.14 (0.08) $\mu$M to 0.55 (0.11) $\mu$M

due to the decomposition of organic matter and dynamic processes (Figure 11c). This change corresponds to the increase in Nit (Amn) term from 0.15 (0.29) to 0.39 (0.36) and has a positive contribution to GppPS. Similarly, the GppPL decrease from 0.57 $\mu$M day$^{-1}$ to 0.02 $\mu$M day$^{-1}$ is not explained by the Sil term from 0.05 to 0.07. The rate of decrease in the Tmp term from 1.25 to 1.04, which derives from the cooling of ocean surface from 3.27 °C to 0.61 °C, is just 20%. The temperature profile higher than the freezing point of about -1.8 °C with remaining temperature maximum at 130 m depth certainly can afford to maintain open water pool at the top of JED. The LA term of 0.32 associated with the NCEP solar radiation of 10 W m$^{-2}$ at the ocean surface assures the continuance of photosynthesis in the available nutrient condition after when sea ice covers the shelf-break region surrounding the JED on October 20. Actually, the LA term decreases from 0.93 on September 19 to 0.06 on October 31 in the open water area. Sea ice concentration then increases from 0 to 1 for November 1 to 9. The daily downward shortwave flux drops to zero (i.e., polar night all the day) owing to solar incidence on November 8 at 73°N. Even taken account for the decrease in PS (PL) biomass itself of 0.19 (0.04) $\mu$M to 0.06 (0.02) $\mu$M, it is indicated that the principal factor for the termination of primary production in spite of nutrient recovery inside the JED is light limitation due to solar incidence rather than sea ice freezing, and surface cooling has secondary contribution.

## 5. Summary and Discussions

The response of phytoplankton to the Beaufort shelf-break eddies in the western Arctic Ocean is examined using the eddy-resolving coupled sea ice-ocean model including a lower trophic marine ecosystem formulation. In the integration from March to November, the reasonable performance on seasonal phytoplankton bloom following sea ice retreat in the shallow Chukchi shelf is achieved. The sea ice margin is located north of the shelf-basin boundary, and several warm eddies are produced during late summer and early autumn. The shelf-break warm eddies initially transports the Chukchi shelf water with high primary productivity toward the Canada Basin interior. In the eddy-developing period, the anti-cyclonic rotational flow along the outer edge of each eddy moving offshore occasionally traps the shelf water. The primary production inside the warm eddies is maintained by internal dynamics in the eddy-maturity period. In particular, the surface central area of an anti-cyclonic eddy satisfies adequate light, nutrient, and warm environment for photosynthetic activity partly attributing to turbulent mixing with underlying nutrient-rich water. The simulated biogeochemical properties with the dominance of small-size phytoplankton inside the warm eddies are consistent with the previous in-situ observation in the western Arctic Ocean. It is also suggested that the light limitation before sea ice freezing rather than nutrient depletion shuts down the primary production in the shelf-break eddies. The findings provided in the present study indicate that the time lag between the phytoplankton bloom in the shelf region following the summertime sea ice retreat and the eddy generation along the Beaufort shelf break is an important index to determine biological regimes in the Canada Basin (Figure 12). When the phytoplankton bloom in the shelf occurs later or continues longer, the shelf-break eddies would further

enhance the primary productivity in the basin interior. Therefore, we propose that the shelf-break eddies play a significant role in the extension of primary production period, the migration of shelf species toward the basin interior, and the bottom-up process of local food web.

There are a lot of uncertainties in zooplankton characteristics, presumably because of insufficient zooplankton measurements. A few model studies incorporated the seasonal vertical migration of Calanus species reported in the subarctic North Pacific [*Aita et al.*, 2003]. While Calanus is categorized as ZL in the NEMURO model, the period and depth of its vertical migration in the Arctic Ocean are specifically unknown and might differ from other regions. That is the reason why the vertical migration process is not included in our experiment. This uncertainty may cause the overestimation of zooplankton biomass described in section 3.2 and consequent high grazing pressure on phytoplankton species. To broadly estimate the impact of zooplankton on the phytoplankton life cycle, we additionally conducted a sensitivity experiment where the initial zooplankton concentration is set to zero. This extreme experiment, whose design is identical to the 2003 case except the removal of zooplankton, is named the "No Zooplankton" (NZOO) case. As expected, the primary productivity in the shelf-break eddies is considerably enhanced in the NZOO case (Figure 13). Thus we regard that the phytoplankton performance is sensitive to the zooplankton behaviors and that the detailed assessment of grazing process should be addressed as our future work. In this connection, the vertically integrated total of GppPS and GppPL at the JED center ranges from 2.30 $\mu$M m day$^{-1}$ ($\sim$ 0.18 gC m$^{-2}$ day$^{-1}$) in the 2003 case to 3.72 $\mu$M m day$^{-1}$ ($\sim$ 0.30 gC m$^{-2}$ day$^{-1}$) in the NZOO case on September 19. The eddy-induced productivity estimated in our experiment is hence below the half of

observed summertime average of 0.78 $\mathrm{gC\,m^{-2}\,day^{-1}}$ in the Chukchi shelf [*Hill and Cota*, 2005] and might have just a minor impact on the pan-Arctic biogeochemical cycle.

The ship-based in-situ measurements have captured the highest ammonium concentration just above the shallow Chukchi shelf [*Nishino et al.*, 2011b]. The dissolution from sea bottom sediments is considered to be a crucial nitrogen source in the shelf region and even in the basin interior throughout the year, although the reliable sequential data has not been acquired yet. Besides, the benthos communities are assumed to be representative consumers of particulate and dissolved organic nitrogen [*Grebmeier et al.*, 2006]. The benthos species might be an important reservoir of nitrogen and possibly modulate ammonium concentration in the deep layer. The ammonium concentration over the Chukchi shelf bottom is assumed to have a distinct seasonal cycle. Actually, the ammonium concentration more than 4 $\mu$M was observed along the northern edge of Chukchi shelf during the summer cruise, while the winter value is below 2 $\mu$M [*Nishino et al.*, 2005]. Our experiment hence applies the restoring method of ammonium concentration with a seasonal cycle as described in section 2. The adopted restoring works on controlling the phase of seasonal variation in the shelf, because we have checked that the experiment without restoring could not reproduce the observed signal in *Nishino et al.* [2005, 2011a]. On the other hand, silicate supply from the shelf bottom is not incorporated because of few observational evidences in the Chukchi Sea. Actually, a major silicate source is suggested to be the Bering Sea rather than bottom sediments [S. Nishino, personal communication]. The silicate inflow from the Bering Sea is indirectly represented by the restoring to WOA09 data at the Bering Strait in the present experiments. The geochemical fluxes from the

548 Chukchi shelf bottom, which have not been quantitatively estimated yet, would be useful
549 information for further model development.

**Acknowledgments**

We would like to express our sincere gratitude to Dr. Shigeto Nishino at the Japan Agency for Marine-Earth Science and Technology (JAMSTEC) for his fruitful comments. This research is funded by Grants-in-Aid for Scientific Research (S) of Japan Society for the Promotion of Science (JSPS) JFY2010-2014, No. 22221003, "Catastrophic reduction of sea ice in the Arctic Ocean: its impact on the marine ecosystems in the polar region". We also appreciate Dr. Naomi Harada at JAMSTEC for the project management. All numerical experiments were executed using the resources of JAMSTEC Earth Simulator version 2. The courteous comments and suggestions of anonymous reviewers markedly benefited the presented product.

## Appendix: Photosynthesis Formulation in NEMURO

The NEMURO model configuration assumes that the photosynthesis of PS and PL is a function of nitrate $NO_3$, ammonium $NH_4$, and silicate $Si(OH)_4$ concentration, water temperature $T$, light intensity $I$ [*Kishi et al.*, 2007]. The formulation of gross primary production rate of PS (GppPS) and PL (GppPL) consists of nitrate, ammonium, silicate uptake terms (Nit, Amn, Sil, respectively), temperature-dependent term (Tmp), and light availability term (LA), and the biomass itself $PS$ and $PL$ as follows:

$$\begin{aligned}
\mathrm{GppPS} \;=\; & \mathrm{V_{maxs}} \left( \underbrace{\frac{NO_3}{NO_3 + \mathrm{K_{NO_3}}} \exp(-\Psi\, NH_4)}_{[\mathrm{Nit}]} + \underbrace{\frac{NH_4}{NH_4 + \mathrm{K_{NH_4}}}}_{[\mathrm{Amn}]} \right) \\
& \underbrace{\exp(\kappa T)}_{[\mathrm{Tmp}]} \underbrace{\frac{I}{\mathrm{I_{opt}}} \exp\left(1 - \frac{I}{\mathrm{I_{opt}}}\right)}_{[\mathrm{LA}]} \underbrace{PS}_{[\mathrm{PS}]}, \\
\mathrm{GppPL} \;=\; & \mathrm{V_{maxl}} \min \left( \frac{NO_3}{NO_3 + \mathrm{K_{NO_3}}} \exp(-\Psi\, NH_4) + \frac{NH_4}{NH_4 + \mathrm{K_{NH_4}}}, \underbrace{\frac{Si(OH)_4}{Si(OH)_4 + \mathrm{K_{Si(OH)_4}}} / \mathrm{RSiN}}_{[\mathrm{Sil}]} \right) \\
& \exp(\kappa T) \frac{I}{\mathrm{I_{opt}}} \exp\left(1 - \frac{I}{\mathrm{I_{opt}}}\right) \underbrace{PL}_{[\mathrm{PL}]},
\end{aligned}$$

where the parameter values of maximum phytosynthetic rate at 0°C $\mathrm{V_{maxs}}$ (0.7 $\mathrm{day^{-1}}$), $\mathrm{V_{maxl}}$ (2.0 $\mathrm{day^{-1}}$), half saturation constant for nitrate $\mathrm{K_{NO_3}}$ (0.7 $\mu$M), ammonium $\mathrm{K_{NH_4}}$ (0.2 $\mu$M), silicate $\mathrm{K_{Si(OH)_4}}$ (1.15 $\mu$M), ammonium inhibition coefficient $\Psi$ (1 $\mu\mathrm{M^{-1}}$), temperature coefficient for photosynthetic rate $\kappa$ (0.0693 $^\circ\mathrm{C^{-1}}$), optimum light intensity constant $\mathrm{I_{opt}}$ (104.7 $\mathrm{W\,m^{-2}}$), and Si:N ratio RSiN of 2 are all given based on *Zhang et al.* [2010]. The nutrient uptake, Tmp, and LA terms are represented by traditional Michaelis-Menten, $\mathrm{Q_{10}}$ relationship, and P-E curve formulation, respectively.

## References

574 Aita, M. N., Y. Yamanaka, and M. J. Kishi, Effects of ontogenetic vertical migration
575 of zooplankton on annual primary production using NEMURO embedded in a general
576 circulation model, *Fish. Oceanogr.*, *12*, 284–290, 2003.

577 Aita, M. N., Y. Yamanaka, and M. J. Kishi, Interdecadal variation of the lower trophic
578 ecosystem in the northern Pacific between 1948 and 2002, in a 3-D implementation of
579 the NEMURO model, *Ecological Modelling*, *202*, 81–94, 2007.

580 Arrigo, K. R., G. van Dijken, and S. Pabi, Impact of a shrinking Arctic ice cover on ma-
581 rine primary production, *Geophys. Res. Lett.*, *35*, L19,603, doi:10.1029/2008GL035,028,
582 2008.

583 Campbell, R. G., E. B. Sherr, C. J. Ashjian, S. Plourde, B. F. Sherr, V. Hill, and D. A.
584 Stockwell, Mesozooplankton prey preference and grazing impact in the western Arctic
585 Ocean, *Deep Sea Res., Part II*, *56*, 1274–1289, 2009.

586 Garcia, H. E., R. A. Locarnini, T. P. Boyer, J. I. Antonov, M. M. Zweng, O. K. Baranova,
587 and D. R. Johnson, World Ocean Atlas 2009, *NOAA Atlas NESDIS*, *4*, 398pp, 2010.

588 Grebmeier, J. M., and H. R. Harvey, The Western Arctic Shelf-Basin Interactions (SBI)
589 project: An overview, *Deep Sea Res., Part II*, *52*, 3109–3115, 2005.

590 Grebmeier, J. M., L. W. Cooper, H. M. Feder, and B. I. Sirenko, Ecosystem dynamics
591 of the Pacific-influenced Northern Bering and Chukchi Seas in the Amerasian Arctic,
592 *Progress in Oceanography*, *71*, 331–361, 2006.

593 Grebmeier, J. M., H. R. Harvey, and D. A. Stockwell, The Western Arctic Shelf-Basin
594 Interactions (SBI) project, volume II: An overview, *Deep Sea Res., Part II*, *56*, 1137–
595 1143, 2009.

596 Grebmeier, J. M., S. E. Moore, J. E. Overland, K. E. Frey, and R. Gradinger, Biological
597 response to recent Pacific Arctic sea ice retreats, *Eos Trans. AGU*, *91*, 161–163, 2010.
598 Hasumi, H., CCSR Ocean Component Model (COCO) version 4.0, *Rep.*, Cent. for Clim.
599 Syst. Res., Tokyo, 2006.
600 Hill, V., and G. Cota, Spatial patterns of primary production on the shelf, slope and basin
601 of the Western Arctic in 2002, *Deep Sea Res., Part II*, *52*, 3344–3354, 2005.
602 Hill, V., G. Cota, and D. Stockwell, Spring and summer phytoplankton communities in
603 the Chukchi and Eastern Beaufort Seas, *Deep Sea Res., Part II*, *52*, 3369–3385, 2005.
604 Jin, M., C. Deal, S. H. Lee, S. Elliott, E. Hunke, M. Maltrud, and N. Jeffery, Investigation
605 of Arctic sea ice and ocean primary production for the period 1992-2007 using a 3-D
606 global ice-ocean ecosystem model, *Deep Sea Res., Part II*, *58*, in press, 2011.
607 Kadko, D., R. S. Pickart, and J. Mathis, Age characteristics of a shelf-break eddy in
608 the western Arctic and implications for shelf-basin exchange, *J. Geophys. Res.*, *113*,
609 C02,018, doi:10.1029/2007JC004,429, 2008.
610 Kalnay, E., M. Kanamitsu, R. Kistler, W. Collins, D. Deaven, L. Gandin, M. Iredell,
611 S. Saha, G. White, J. Woolen, Y. Zhu, M. Chelliah, W. Ebisuzaki, W. Higgins,
612 J. Janowiak, K. C. Mo, C. Ropelewski, J. Wang, A. Leetmaa, R. Reynolds, R. Jenne,
613 and D. Joseph, The NCEP/NCAR 40-year reanalysis project, *Bull. Amer. Meteor. Soc.*,
614 *77*, 437–471, 1996.
615 Kawasaki, T., and H. Hasumi, Role of localized mixing around the Kuril
616 Straits in the Pacific thermohaline circulation, *J. Geophys. Res.*, *115*, C11,002,
617 doi:10.1029/2010JC006,130, 2010.

Kishi, J. M., M. Kashiwai, D. M. Ware, B. A. Megrey, D. L. Eslinger, F. E. Werner, M. Noguchi-Aita, T. Azumaya, M. Fujii, S. Hashimoto, D. Huang, H. Iizumi, Y. Ishida, S. Kang, G. A. Kantakov, H. Kim, K. Komatsu, V. V. Navrotsky, S. L. Smith, K. Tadokoro, A. Tsuda, O. Yamamura, Y. Yamanaka, K. Yokouchi, N. Yoshie, J. Zhang, Y. I. Zuenko, and V. I. Zvalinsky, NEMURO - a lower trophic level model for the North Pacific marine ecosystem, *Ecological Modelling*, *202*, 12–25, 2007.

Kishi, M. J., S. Itoh, B. A. Megrey, K. A. Rose, and F. E. Werner, A review of the NEMURO and NEMURO.FISH models and their application to marine ecosystem investigations, *J. Oceanogr.*, *67*, 3–16, 2011.

Lee, S. H., T. E. Whitledge, and S.-H. Kang, Recent carbon and nitrogen uptake rates of phytoplankton in Bering Strait and the Chukchi Sea, *Continental Shelf Res.*, *27*, 2231–2249, 2007.

Manley, T. O., and K. Hunkins, Mesoscale eddies of the Arctic Ocean, *J. Geophys. Res.*, *90*, 4911–4930, 1985.

Mathis, J. T., R. S. Pickart, D. A. Hansell, D. Kadko, and N. R. Bates, Eddy transport of organic carbon and nutrients from the Chukchi Shelf: Impact on the upper halocline of the western Arctic Ocean, *J. Geophys. Res.*, *112*, C05,011, doi:10.1029/2006JC003,899, 2007.

National Ice Center, National Ice Center Arctic sea ice charts and climatologies in gridded format, *Digital Media*, National Snow and Ice Data Center, Boulder, Colorado, 2006.

Nishino, S., K. Shimada, and M. Itoh, Use of ammonium and other nitrogen tracers to investigate the spreading of shelf waters in the western Arctic halocline, *J. Geophys. Res.*, *110*, C10,005, doi:10.1029/2003JC002,118, 2005.

Nishino, S., M. Itoh, Y. Kawaguchi, T. Kikuchi, and M. Aoyama, Impact of an unusually large warm-core eddy on distributions of nutrients and phytoplankton in the southwestern Canada Basin during late summer/early fall 2010, *Geophys. Res. Lett.*, *38*, L16,602, doi:10.1029/2011GL047,885, 2011a.

Nishino, S., T. Kikuchi, M. Yamamoto-Kawai, Y. Kawaguchi, T. Hirawake, and M. Itoh, Enhancement/reduction of biological pump depends on ocean circulation in the sea-ice reduction regions of the Arctic Ocean, *J. Oceanogr.*, *67*, 305–314, 2011b.

Noh, Y., and H. J. Kim, Simulations of temperature and turbulence structure of the oceanic boundary layer with the improved near-surface process, *J. Geophys. Res.*, *104*, 15,621–15,634, 1999.

Okkonen, S. R., T. J. Weingartner, S. L. Danielson, D. L. Musgrave, and G. M. Schmidt, Satellite and hydrographic observations of eddy-induced shelf-slope exchange in the northwestern Gulf of Alaska, *J. Geophys. Res.*, *108*, C23,033, doi:10.1029/2002JC001,342, 2003.

Pabi, S., G. L. van Dijken, and K. R. Arrigo, Primary production in the Arctic Ocean, 1998-2006, *J. Geophys. Res.*, *113*, C08,005, doi:10.1029/2007JC004,578, 2008.

Palmer, M. A., K. R. Arrigo, C. J. Mundy, J. K. Ehn, M. Gosselin, D. G. Barber, J. Martin, E. Alou, S. Roy, and J.-E. Tremblay, Spatial and temporal variation of photosynthetic parameters in natural phytoplankton assemblages in the Beaufort Sea, Canadian Arctic, *Polar Biol.*, *34*, 1915–1928, 2011.

Pickart, R. S., Shelfbreak circulation in the Alaskan Beaufort Sea: Mean structure and variability, *J. Geophys. Res.*, *109*, C04,024. doi:10.1029/2003JC001,912, 2004.

663 Popova, E. E., A. Yool, A. C. Coward, Y. K. Aksenov, S. G. Alderson, B. A. de Cuevas,
664 and T. R. Anderson, Control of primary production in the Arctic by nutrients and
665 light: insights from a high resolution ocean general circulation model, *Biogeosciences*,
666 *7*, 3569–3591, 2010.

667 Spall, M. A., R. S. Pickart, P. S. Fratantoni, and A. J. Plueddemann, Western Arctic
668 shelfbreak eddies: Formation and transport, *J. Phys. Oceanogr.*, *38*, 1644–1668, 2008.

669 Steele, M., R. Morley, and W. Ermold, PHC: A global ocean hydrography with a high-
670 quality Arctic Ocean, *J. Climate*, *14*, 2079–2087, 2001.

671 Sukhanova, I. N., M. V. Flint, L. A. Pautova, D. A. Stockwell, J. M. Grebmeier, and
672 V. M. Sergeeva, Phytoplankton of the western Arctic in the spring and summer of 2002:
673 Structure and seasonal changes, *Deep Sea Res., Part II*, *56*, 1223–1236, 2009.

674 Sumata, H., T. Hashioka, T. Suzuki, N. Yoshie, T. Okunishi, M. N. Aita, T. T. Sakamoto,
675 A. Ishida, N. Okada, and Y. Yamanaka, Effect of eddy transport on the nutrient supply
676 into the euphotic zone simulated in an eddy-permitting ocean ecosystem model, *J. Mar.*
677 *Sys.*, *83*, 67–87, 2010.

678 Ueno, H., W. R. Crawford, and H. Onishi, Impact of Alaskan Stream eddies on chlorophyll
679 distribution in the North Pacific, *J. Oceanogr.*, *66*, 319–328, 2010.

680 Walsh, J. J., D. A. Dieterle, F. R. Chen, J. M. Lenes, W. Maslowski, J. J. Cassano,
681 T. E. Whitledge, D. Stockwell, M. Flint, I. N. Sukhanova, and J. Christensen, Trophic
682 cascades and future harmful algal blooms within ice-free Arctic Seas north of Bering
683 Strait: A simulation analysis, *Prog. Oceanogr.*, *91*, 312–343, 2011.

684 Wang, J., G. F. Cota, and J. C. Comiso, Phytoplankton in the Beaufort and Chukchi
685 Seas: Distribution, dynamics, and environmental forcing, *Deep Sea Res., Part II*, *52*,

3355–3368, 2005.

Watanabe, E., Beaufort shelf break eddies and shelf-basin exchange of Pacific summer water in the western Arctic Ocean detected by satellite and modeling analyses, *J. Geophys. Res.*, *116*, C08,034, doi:10.1029/2010JC006,259, 2011.

Watanabe, E., Linkages among halocline variability, shelf-basin interaction, and wind regimes in the Beaufort Sea demonstrated in pan-Arctic Ocean modeling framework, *submitted to Ocean Modelling*, 2012.

Watanabe, E., and H. Hasumi, Pacific water transport in the western Arctic Ocean simulated by an eddy-resolving coupled sea ice-ocean model, *J. Phys. Oceanogr.*, *39*, 2194–2211, 2009.

Weingartner, T., K. Aagaard, R. Woodgate, S. Danielson, Y. Sasaki, and D. Cavalieri, Circulation on the north central Chukchi Sea shelf, *Deep Sea Res., Part II*, *52*, 3150–3174, 2005.

Zhang, J., Y. H. Spitz, M. Steele, C. Ashjian, R. Campbell, L. Berline, and P. Matrai, Modeling the impact of declining sea ice on the Arctic marine planktonic ecosystem, *J. Geophys. Res.*, *115*, C10,015, doi:10.1029/2009JC005,387, 2010.

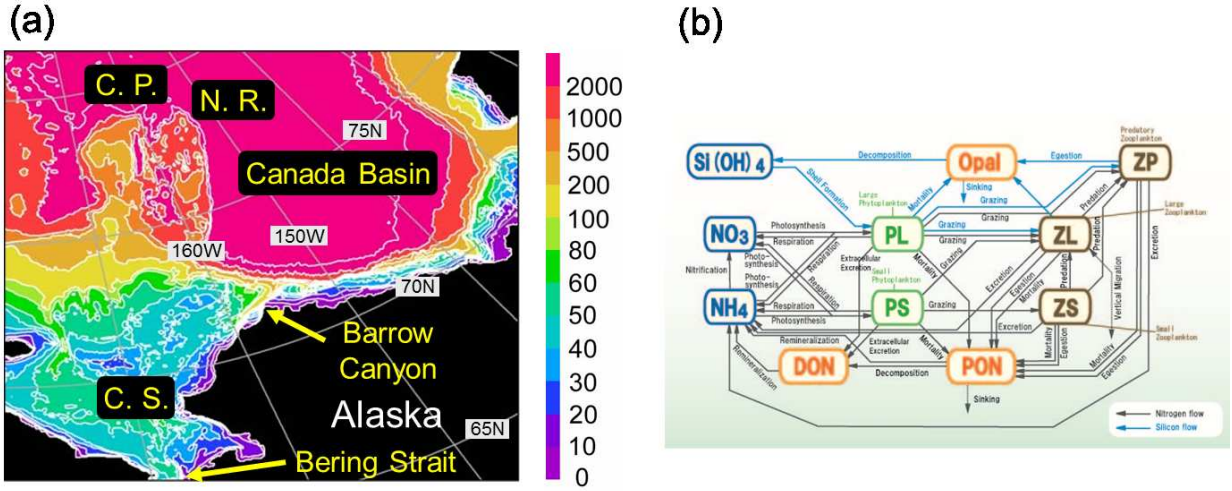


**Figure 1.** (a) Model bathymetry [m]. The locations include Chukchi Sea (C.S.), Chukchi Plateau (C.P.), and Northwind Ridge (N.R.). (b) NEMURO is composed of small phytoplankton (PS), large phytoplankton (PL), small zooplankton (ZS), large zooplankton (ZL), predatory zooplankton (ZP), nitrate ($NO_3$), ammonium ($NH_4$), silicate ($Si(OH)_4$), opal (Opal), particulate organic nitrogen (PON), and dissolved organic nitrogen (DON). PL and PS are assumed to represent diatom and other non-diatom group (e.g., flagellates, haptophytes), respectively.

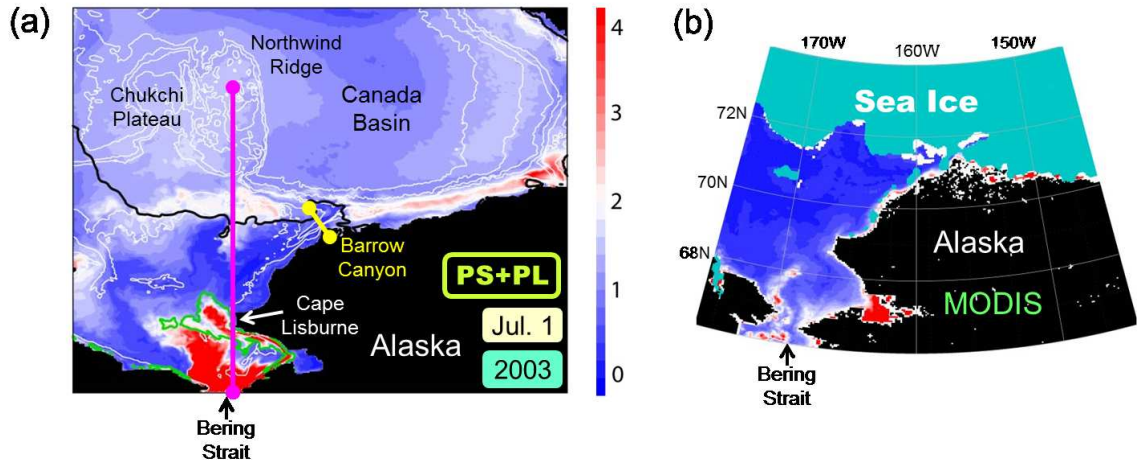


**Figure 2.** (a) Surface phytoplankton concentration on July 1 in the 2003 case [$\mu$M]. Sum of PS and PL is shaded, and PS concentration of 0.1 $\mu$M is plotted by green contours. Black contour shows the simulated sea ice concentration of 0.5 on the same day. White contours show bottom bathymetry. Pink line connected between the Bering Strait and the Northwind Ridge is referred in Figure 3. Yellow line across the Barrow Canyon is referred in Figures 4 and 5. (b) MODIS monthly composite of chlorophyll-$a$ (CHL) concentration in July 2003. Scene ID is A20031822003212. MODIS values with the unit of mgChl m$^{-3}$ are divided by 1.6 to directly compare the simulated PS and PL concentration. AMSR-E sea ice area is overlaid by sky-blue shade.

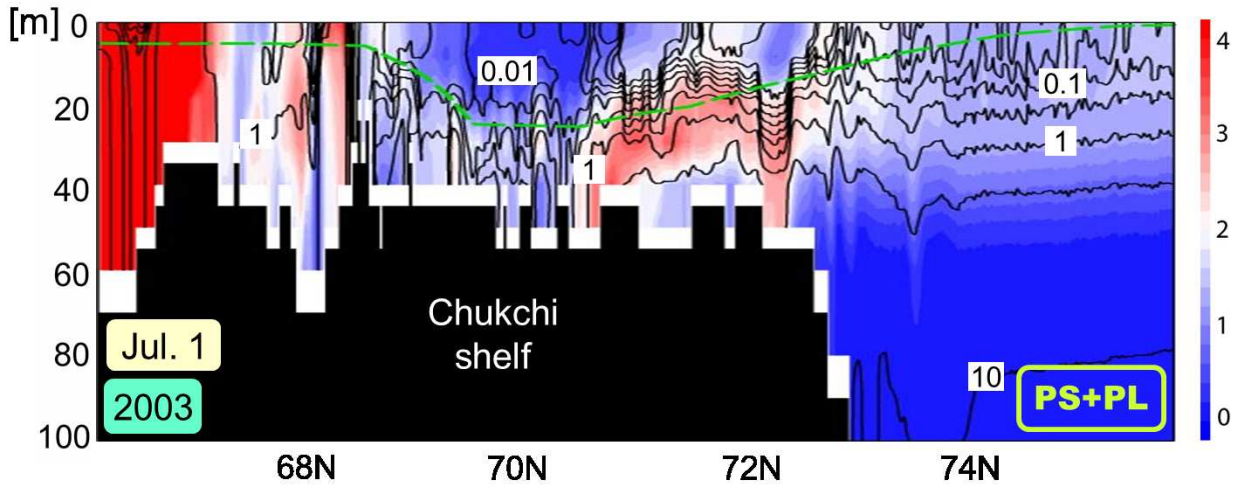


**Figure 3.** Vertical profile of combined PS and PL concentration along the meridional section from the Bering Strait to the Northwind Ridge (a pink line in Figure 2a) on July 1 in the 2003 case. Black contours show the simulated nitrate concentration with logarithm scale. Unit of both the properties is $\mu$M. WOA09 July climatology of nitrate concentration of 1 $\mu$M is overlaid by a green dashed line.

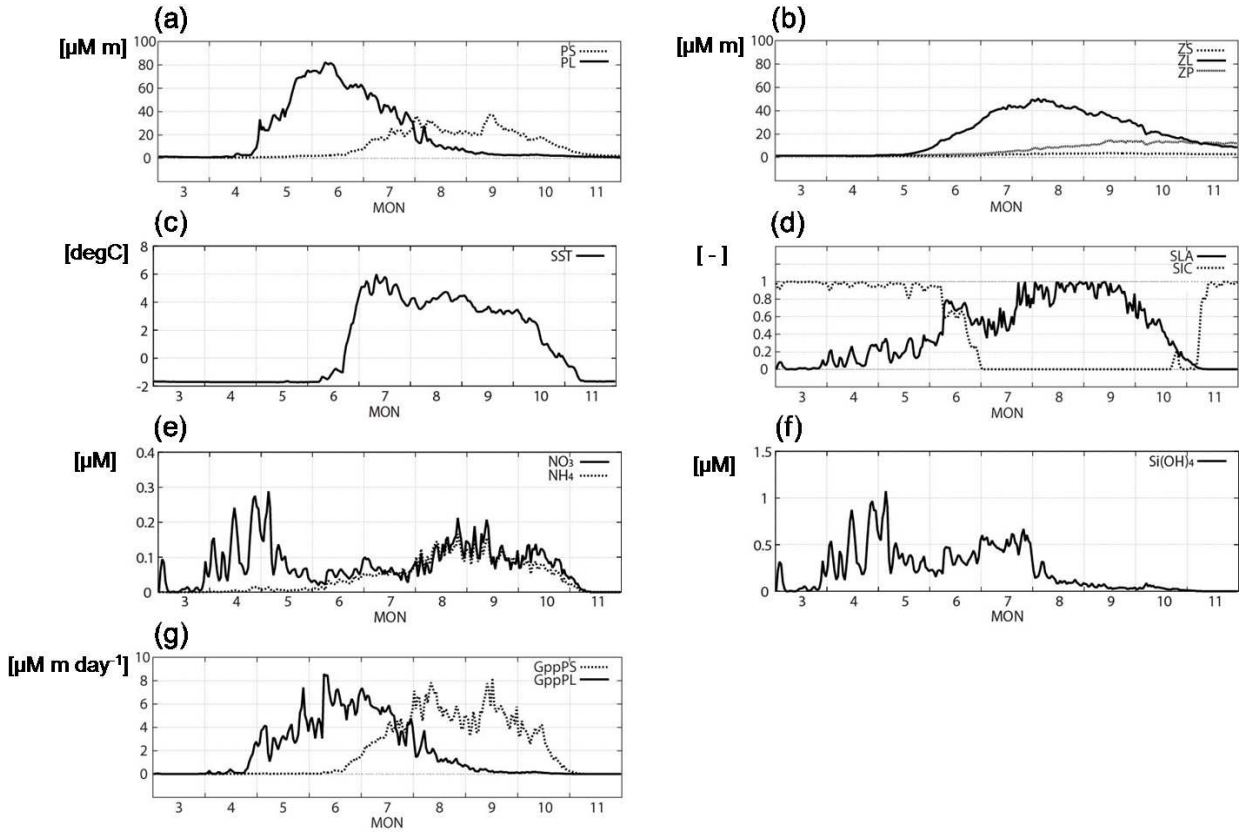


**Figure 4.** Seasonal variations in simulated biogeochemical and physical properties averaged in the Barrow Canyon section (a yellow line in Figure 2a) in the 2003 case. (a) PS, PL, (b) ZS, ZL, and ZP biomass integrated in the entire water column [$\mu$M m]. (c) Sea surface temperature (SST) [°C]. (d) Surface light availability (SLA) and sea ice concentration (SIC) [non-dimension]. (e) $NO_3$, $NH_4$, and (f) $Si(OH)_4$ concentration weighted by light availability [$\mu$M]. As for the unit of $Si(OH)_4$, $1\,\mu\mathrm{M} \equiv 1\,\mathrm{mmolSi\,m^{-3}}$ is assumed. (g) Gross primary production rate of PS (GppPS) and PL (GppPL) [$\mu\mathrm{M\,m\,day^{-1}}$]. See their definition in section 3.2.

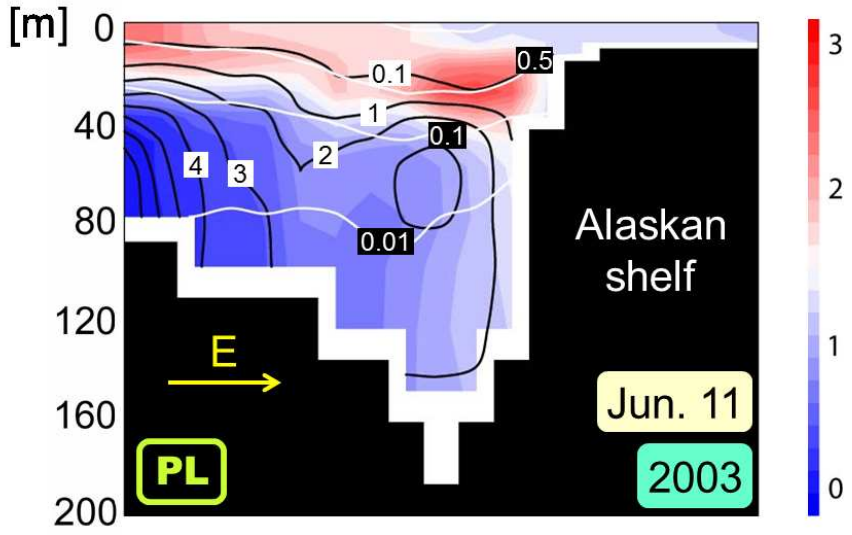


**Figure 5.** Color shade indicates the vertical profile of PL concentration along the Barrow Canyon section on June 11 in the 2003 case [$\mu$M]. Black and white contours show the simulated nitrate concentration [$\mu$M] and light availability [non-dimension], respectively.

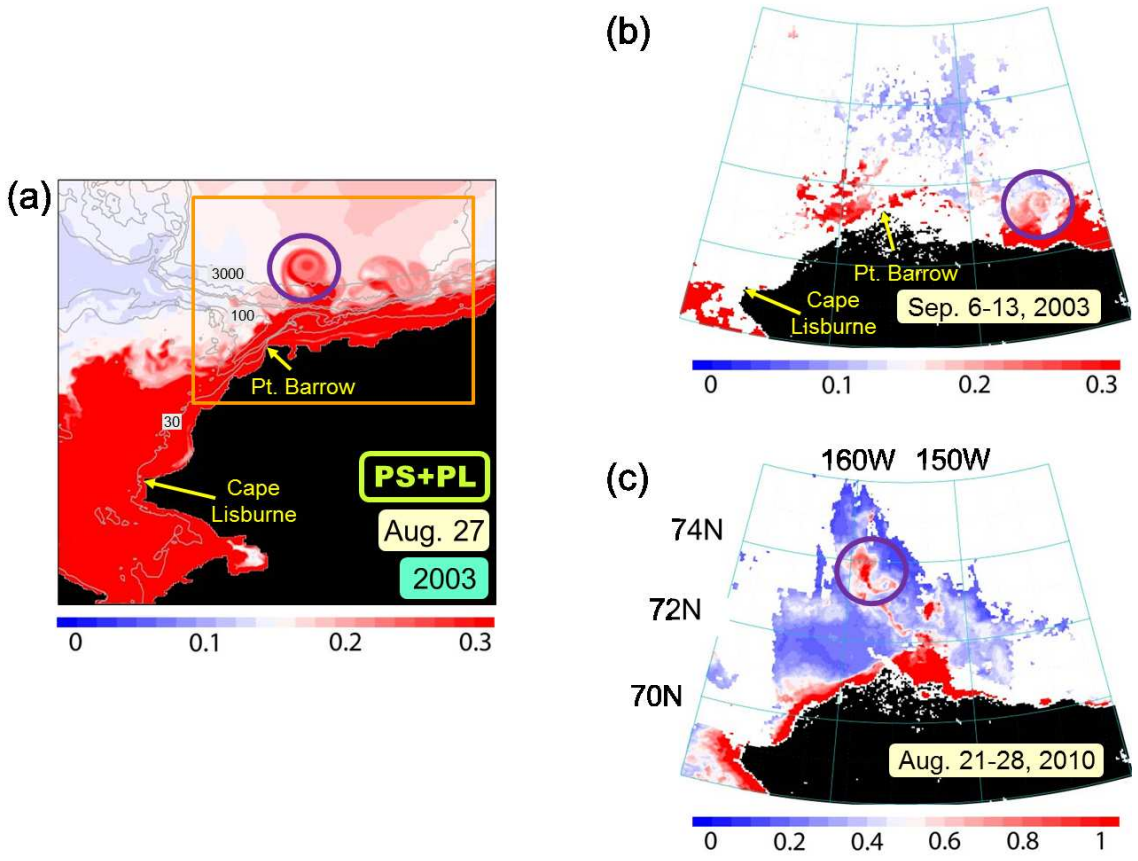


**Figure 6.** (a) Surface combined PS and PL concentration on August 27 in the 2003 case [$\mu$M]. Gray contours denote the water depths of 30, 60, 100, 500, 1000, 2000, and 3000 m. Orange rectangle is a target region in Figures 7, 8, and 13. MODIS 8-day composites of CHL concentration on (b) September 6 - 13, 2003 and (c) August 21 - 28, 2010. Scene ID is (b) A20032492003256 and (c) A20102332010240. MODIS values with the unit of mgChl $\mathrm{m}^{-3}$ are divided by 1.6 to directly compare the simulated PS and PL concentration. Eddy-like CHL patterns are captured in purple circles.

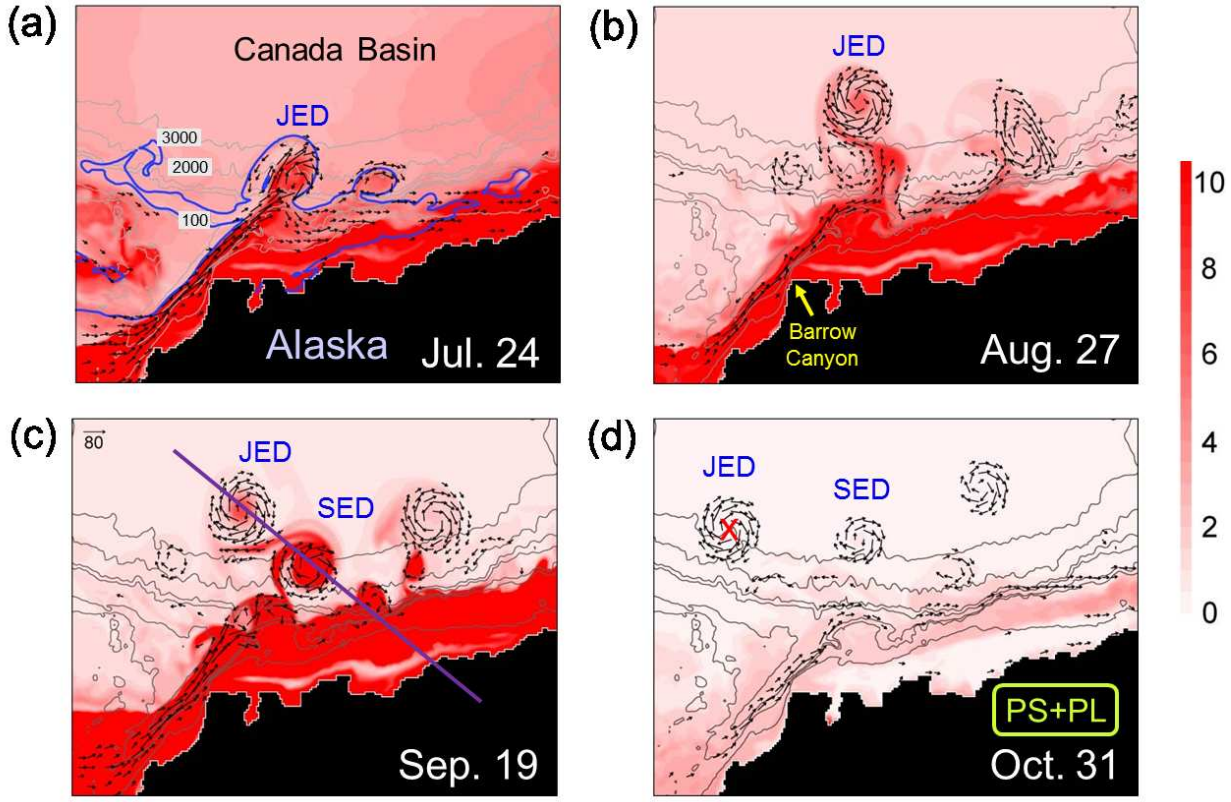


**Figure 7.** (Shade) Sum of GppPS and GppPL [$10^{-2}\,\mu$M day$^{-1}$] and (vectors) horizontal velocity at the ocean surface on (a) July 24, (b) August 27, (c) September 19, and (d) October 31. Unit vector of ocean velocity in (c) is 80 cm s$^{-1}$, and vectors of velocity below 20 cm s$^{-1}$ are hidden. See Figure 6a for each displayed region and gray contours. Surface concentration of Pacific water tracer is 0.1 along blue contours in (a). Purple line across July Eddy (JED) and September Eddy (SED) in (c) is referred in Figures 9 and 10. Red cross in (d) is referred in Figure 11.

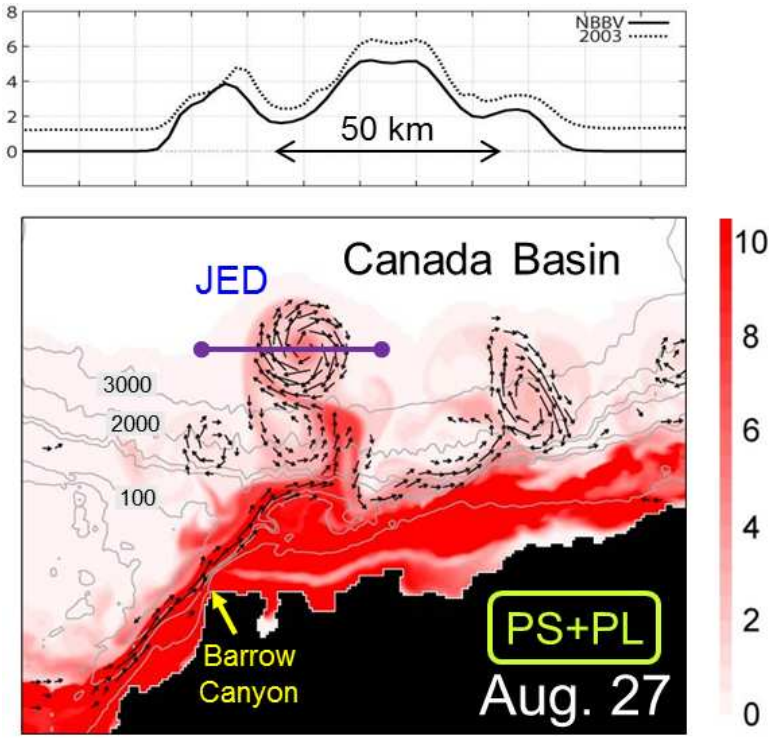


**Figure 8.** Same as Figure 7b, but in the NBBV case. Top figure shows the sum of surface GppPS and GppPL in the (solid line) 2003 and (dashed line) NBBV cases along a purple line in the bottom figure [$10^{-2}\,\mu$M day$^{-1}$].

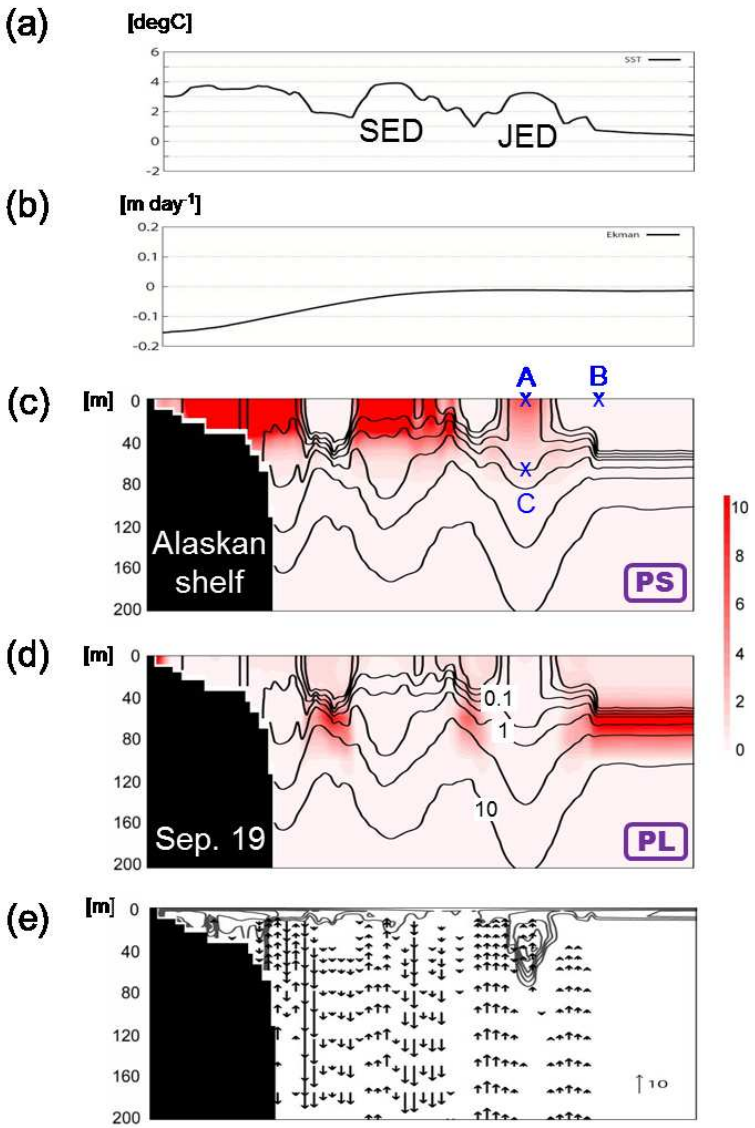


**Figure 9.** Profiles along a purple line in Figure 7c on September 19 in the 2003 case. (a) SST [°C] and (b) Ekman upwelling/downwelling calculated from surface wind stress [m day$^{-1}$]. (c) GppPS and (d) GppPL [$10^{-2}$ $\mu$M day$^{-1}$]. Nitrate concentration is overlaid by contours in (c-d) [$\mu$M]. (e) (contours) Vertical diffusivity diagnosed by the turbulence mixing scheme and (vectors) vertical velocity. Contour interval is 50 cm$^2$ s$^{-1}$. Unit vector of velocity is 10 m day$^{-1}$, and vectors of velocity below 1 m day$^{-1}$ are hidden. Locations of surface eddy center, surface eddy edge, and subsurface eddy center are labeled as A, B, and C, respectively.

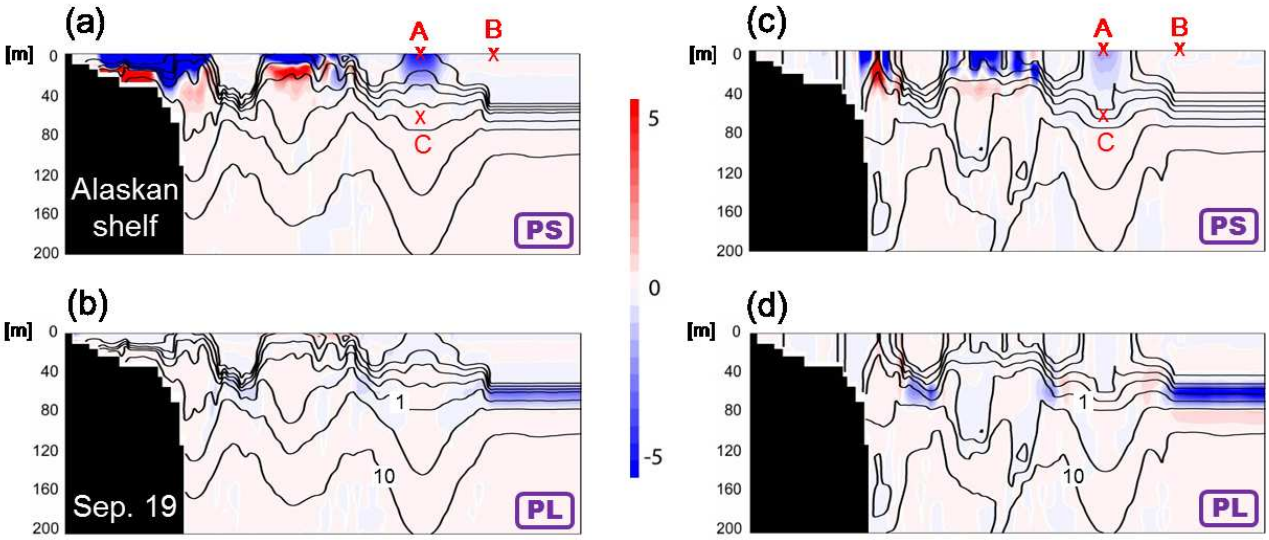


**Figure 10.** Same as (a,c) Figure 9c and (b,d) Figure 9d, but their anomalies in the (a-b) NVND and (c-d) NVNA cases, respectively, from the 2003 case.

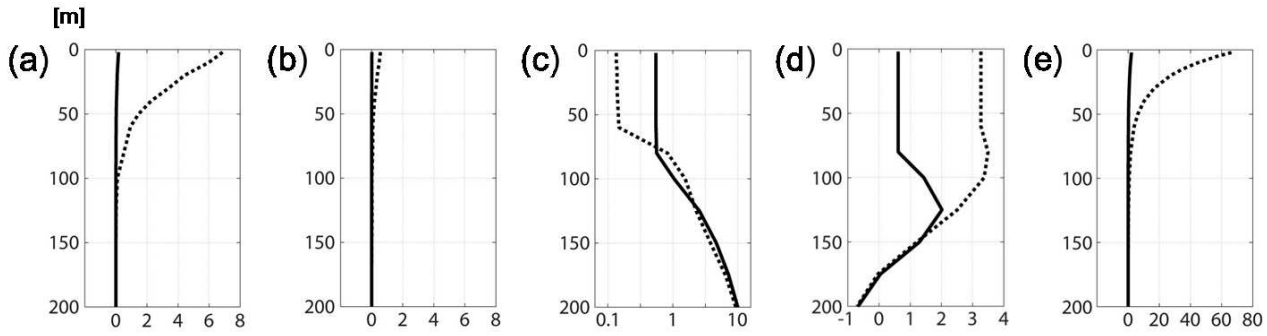


**Figure 11.** Vertical profiles at the JED center on (dashed line) September 19 and (solid line) October 31 in the 2003 case. See the exact location in Figure 7d. (a) GppPS and (b) GppPL [$10^{-2}\,\mu$M day$^{-1}$]. (c) Nitrate concentration with logarithm scale [$\mu$M], (d) water temperature [°C], and (e) light intensity [W m$^{-2}$].

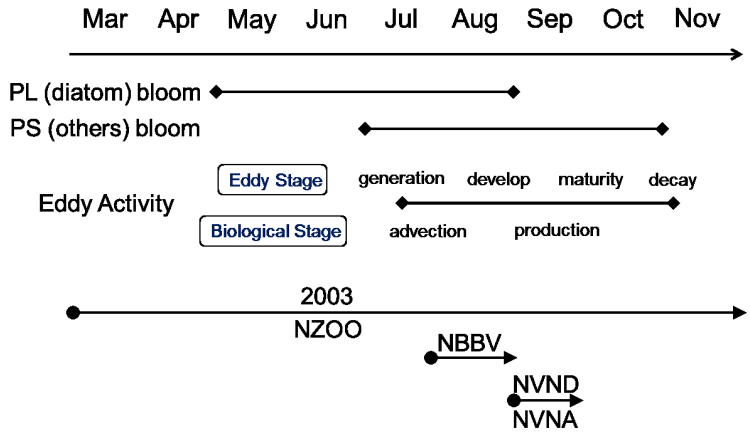


**Figure 12.** Time lag between phytoplankton bloom in the Chukchi shelf and eddy activity in the Beaufort shelf-break region. Integration periods in each experiment are also attached.

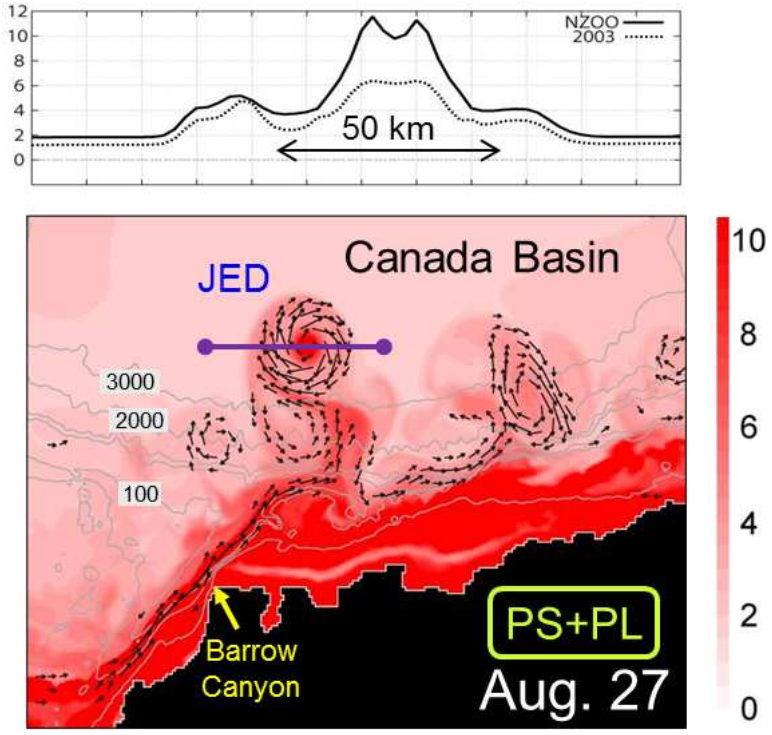


**Figure 13.** Same as Figure 8, but in the NZOO case.

**Table 1.** GppPS, GppPL [$10^{-2}\,\mu$M day$^{-1}$], PS, PL [$\mu$M], $NO_3$, $NH_4$, $Si(OH)_4$ [$10^{-2}\,\mu$M], T [°C], and I [W m$^{-2}$] at surface eddy center, surface eddy edge, and subsurface eddy center in Figures 9c-d and 10. Values of each term of photosynthesis formulation (Nit, Amn, Sil, Tmp, LA) are also presented.

| [2003] | | Surface Eddy Center | Surface Eddy Edge | Subsurface Eddy Center |
|---|---|---|---|---|
| GppPS | | 6.86 | 0.01 | 0.93 |
| GppPL | | 0.57 | 0.70 | 0.08 |
| PS | | 0.19 | 0.01 | 0.18 |
| PL | | 0.04 | 0.09 | 0.04 |
| $NO_3$ | (Nit) | 13.55 (0.15) | 0.20 (0.00) | 14.76 (0.16) |
| $NH_4$ | (Amn) | 8.06 (0.29) | 0.81 (0.04) | 9.01 (0.31) |
| $Si(OH)_4$ | (Sil) | 6.59 (0.05) | 267.89 (0.70) | 6.92 (0.06) |
| T | (Tmp) | 3.27 (1.25) | 0.70 (1.05) | 3.27 (1.25) |
| I | (LA) | 66.26 (0.93) | 66.30 (0.93) | 3.81 (0.12) |

| [NVND] | | Surface Eddy Center | Surface Eddy Edge | Subsurface Eddy Center |
|---|---|---|---|---|
| GppPS | | 1.64 | 0.01 | 1.43 |
| GppPL | | 0.21 | 0.61 | 0.18 |
| PS | | 0.13 | 0.01 | 0.13 |
| PL | | 0.04 | 0.09 | 0.04 |
| $NO_3$ | (Nit) | 1.53 (0.02) | 0.14 (0.00) | 60.47 (0.36) |
| $NH_4$ | (Amn) | 3.19 (0.14) | 0.72 (0.03) | 24.96 (0.56) |
| $Si(OH)_4$ | (Sil) | 2.64 (0.02) | 286.52 (0.71) | 16.01 (0.12) |
| T | (Tmp) | 3.27 (1.25) | 0.70 (1.05) | 3.27 (1.25) |
| I | (LA) | 66.63 (0.93) | 66.30 (0.93) | 4.44 (0.14) |

| [NVNA] | | Surface Eddy Center | Surface Eddy Edge | Subsurface Eddy Center |
|---|---|---|---|---|
| GppPS | | 5.12 | 0.01 | 0.74 |
| GppPL | | 0.44 | 0.71 | 0.06 |
| PS | | 0.17 | 0.01 | 0.16 |
| PL | | 0.04 | 0.09 | 0.04 |
| $NO_3$ | (Nit) | 8.95 (0.11) | 0.20 (0.00) | 9.53 (0.11) |
| $NH_4$ | (Amn) | 7.41 (0.27) | 0.82 (0.04) | 8.24 (0.29) |
| $Si(OH)_4$ | (Sil) | 5.36 (0.04) | 260.37 (0.69) | 5.64 (0.05) |
| T | (Tmp) | 3.27 (1.25) | 0.70 (1.05) | 3.27 (1.25) |
| I | (LA) | 66.41 (0.93) | 66.30 (0.93) | 4.05 (0.13) |